Ocean and Coastal Management 272 (2026) 108004

Contents lists available at ScienceDirect

Ocean and Coastal Management

journal homepage: www.elsevier.com/locate/ocecoaman

Nature's double defense: How mangroves and intertidal topography shape coastal flood mitigation

Rizhong Huang [a], Zhan Tian [b,*], Dongli Fan [a,**], Qinghua Ye [c,d], Qiaodan Liu [e], Ming Kong [b], Yanlong Wang [b], Jiajie Lyu [b], Laixiang Sun [f]

[a] Faculty of Chemical and Engineering and Energy Technology, Shanghai Institute of Technology, Shanghai, 201418, China
[b] School of Environmental Science and Engineering, Southern University of Science and Technology, Shenzhen, 518055, China
[c] Deltares, Delft, the Netherlands
[d] Department of Hydraulic Engineering, Faculty of Civil Engineering and Geosciences, Delft University of Technology, Delft, the Netherlands
[e] Department of Urbanism, Faculty of Architecture and the Built Environment, Delft University of Technology, Delft, the Netherlands
[f] Department of Geographical Sciences, University of Maryland, College Park, MD, 20742, USA

ARTICLE INFO

Keywords:
Mangrove
Intertidal topography
Nature-based solutions (NbS)
Coastal flood risk
Hydrodynamic model

ABSTRACT

Coastal cities increasingly face compound flooding risks due to sea-level rise and intensifying storms. This study systematically evaluates the synergistic regulation of coastal hydrodynamics by mangrove vegetation and intertidal topography as a nature-based solution (NbS) for coastal defense. Based on the Delft3D Flexible Mesh (FM) system, we simulate tidal and storm surge scenarios in two contrasting shorelines in Shenzhen, China, the naturally evolved Xiwan Mangrove Park and the engineered Bao'an Airport coastline. Results show that intertidal topography plays a dominant role in attenuating flow velocity, while mangrove vegetation becomes the primary factor in reducing peak water levels during extreme events. A functional shift in mitigation zones occurs, from mid and low tidal flats under tidal conditions to high flats during storm surges, driven by increased inundation and canopy engagement. Additionally, a clear design threshold of 600 m planting width is identified, beyond which additional vegetation provides diminishing returns due to the complete submergence of mangrove vegetation. These findings underscore the complementary roles of topography and vegetation and offer actionable guidance for optimizing NbS strategies in site-specific, climate-adaptive coastal management.

1. Introduction

Coastal megacities in low-lying deltas are increasingly exposed to compound flooding risks caused by sea-level rise, stronger storm surges, and changing precipitation patterns associated with climate change (Menéndez et al., 2019; Ward et al., 2018; Gilman et al., 2008; Emanuel, 2005). Traditional gray infrastructure, including seawalls and levees, often lacks the flexibility, adaptability, and ecological co-benefits required to address these evolving hazards (Hagger et al., 2022; Chan et al., 2021; De Dominicis et al., 2020; Reguero et al., 2018). As a result, Nature-based Solutions (NbS) are receiving growing attention for their ability to reduce coastal risks while also enhancing biodiversity (Wei et al., 2024, 2025), supporting carbon sequestration (Sasmito et al., 2025; Zhang et al., 2025; Chen et al., 2018; Bouillon et al., 2008) and delivering economic benefits through shoreline protection and ecosystem services (Menéndez et al., 2020; Hochard et al., 2019; Temmerman et al., 2013). Among the range of NbS strategies, mangrove vegetation and intertidal topography are two fundamental but distinct forms of natural defense. Mangroves reduce wave and surge energy through canopy drag, while intertidal topography shapes flow patterns through elevation gradients and bed friction (Krauss et al., 2014; Das and Vincent, 2009; Mazda et al., 2006; Stark et al., 2016). Despite their complementary roles, the synergistic potential of these dual mechanisms remains largely unexplored in both theoretical frameworks and practical implementations.

Existing research on the hydrodynamic functions of mangroves typically employs three complementary approaches: in situ observations (Horstman et al., 2014), laboratory flume experiments (Maza et al., 2017), and numerical hydrodynamic modeling (Chen et al., 2021). For example, Zhou et al. (2022a) documented a nearly linear decay of wave

* Corresponding author.
** Corresponding author.
E-mail addresses: tianz@sustech.edu.cn (Z. Tian), fandl@sit.edu.cn (D. Fan).

https://doi.org/10.1016/j.ocecoaman.2025.108004
Received 21 July 2025; Received in revised form 23 September 2025; Accepted 1 November 2025
Available online 10 November 2025

height through mangroves during a typhoon, with attenuation strongly modulated by water depth and forest structure. Using near-prototype flume tests with 3D-printed Rhizophora analogs, Chang et al. (2022) demonstrated that the complex root architecture substantially increases wave-induced drag. In regional modeling study of the Pearl River Delta, De Dominicis et al. (2023) showed that mangrove-belt width, vegetation drag coefficients, and spatial configuration jointly drive storm-surge attenuation, as illustrated during Typhoon Hato.

Despite these advances, most studies consider either mangrove vegetation or intertidal topography in isolation, with few addressing their coupled, spatially explicit interactions (Kiesel et al., 2022; Maza et al., 2019). This disconnect overlooks the ways in which tidal flat elevation, slope gradients, and subzone heterogeneity modulate vegetation performance under varying hydrodynamic regime. Moreover, few models differentiate the hydrodynamic responses of high, mid, and low tidal flats, even though field evidence demonstrates that surge attenuation and flow resistance vary significantly with elevation and inundation depth (Smolders et al., 2015; Liu et al., 2013). The absence of elevation-stratified modeling constrains our understanding of how drag dynamics and protective capacity shift under different forcing conditions, particularly during extreme storm events when higher tidal zones become inundated (Lagomasino et al., 2021; Alongi, 2008).

Additionally, mangrove belt width is widely recognized as a key factor influencing mitigation performance (Zhang et al., 2012; Mazda et al., 1997). However, most studies have not identified design thresholds beyond which additional planting provides little extra benefit. Similarly, few studies have assessed how the marginal effectiveness of comparable natural-based solutions differs between natural and engineered shorelines. Natural coasts with mangrove-fringed tidal flats dissipate waves and currents while offering ecological co-benefits, whereas engineered coasts rely on hard infrastructure that lacks such multifunctionality. The role of tides is likewise context-dependent: under normal conditions, tides modulate day-to-day wave and flow dynamics; during extreme events, they interact with storm surges to reshape inundation patterns and condition the performance of coastal defenses. These gaps underscore the need for spatially explicit, mechanism-based assessments of how mangroves and intertidal topography jointly regulate coastal hydrodynamics across both routine and extreme forcing.

To address these gaps, we investigate how mangrove vegetation and intertidal topography jointly regulate coastal hydrodynamics under tidal and storm-surge forcing. Using the Delft3D Flexible Mesh (FM) system, we simulate two representative coastlines in Shenzhen to quantify their individual and combined effects on flow velocity and water level. The findings provide practical guidance for optimizing nature-based strategies for coastal flood mitigation.

This study makes three key contributions. First, it explicitly evaluates the coupled effects of mangroves and intertidal topography, addressing a gap where these factors are often examined in isolation. Second, it applies a scenario-based Delft3D FM framework to quantify their individual and joint influences on flow velocity and water level under tidal and storm-surge forcing. Third, it identifies design-relevant thresholds and site-specific insights to support planning and optimization of climate-adaptive, cost-effective, nature-based coastal defenses.

2. Materials and methods

2.1. Study area

Shenzhen, located on the eastern coast of the Pearl River Delta in southern China, has experienced rapid urbanization since the establishment of its Special Economic Zone in 1980. As one of the country's most economically dynamic cities, it has undergone extensive land reclamation and coastal modification, which have significantly altered shoreline morphology and degraded natural ecosystems, particularly mangrove wetlands (Wang et al., 2021; Ai et al., 2020).

With the ongoing impacts of climate change, including sea-level rise and increasing storm surge frequency, Shenzhen's coastal areas face heightened flood risk. The city is currently among the most vulnerable globally to sea-level rise, with projections indicating a further increase in exposure by 2050 (Hallegatte et al., 2013). In response, the Shenzhen municipal government has initiated multiple NbS programs focused on mangrove restoration and ecological rehabilitation (Su et al., 2021; Hu et al., 2020; Peng et al., 2016).

This study examines two representative coastal reaches in Shenzhen: (i) Xiwan Mangrove Park (Bao'an District), with extensive natural tidal flats and mature mangrove stands; and (ii) the Bao'an Airport coastline along the northwestern Pearl River Estuary, characterized by low-lying reclaimed land with minimal vegetated buffering and reliance on hard defenses (see Fig. 1). The estuary exhibits irregular semidiurnal tides with a mean range of 0.8–1.6 m, amplified landward during spring tides. Local hydrodynamics are further modulated by estuarine circulation and river discharge, and episodically by typhoon-induced storm surges, producing strong spatiotemporal variability in water levels and currents. These contrasting geomorphic and hydrodynamic settings provide a robust basis for evaluating NbS performance under different coastal conditions.

2.2. Hydrodynamic model configuration and validation

A tidal and storm surge hydrodynamic model was developed using the Delft3D FM system, covering the South China Sea and the Pearl River Estuary. The model employs an unstructured computational grid composed of triangular and quadrilateral cells, enabling accurate representation of complex coastlines and hydrodynamic boundaries. Grid resolution is approximately 75 m in nearshore areas, gradually expanding to 500–10,000 m toward the open ocean, resulting in 118,258 computational elements. This configuration ensures a balance between computational efficiency and simulation accuracy. Key model parameters are summarized in Table 1.

The model is based on the hydrostatic assumption and incorporates baroclinic pressure gradients induced by temperature and salinity variations to simulate density-driven circulation. Tidal forcing is applied at the open boundaries using water level data derived from the Delft Global Tide Model (GSTM) and the FES2012 model. Boundary conditions for temperature and salinity are obtained from reanalysis datasets provided

Table 1
Key parameter settings used in the three-dimensional hydrodynamic model.

Param Description	Param Name	Value
Maximum number of vertical layers	Kmx	20
Vertical layering type	Laverttype	Sigma layer
Layer thickness distribution	StretchType	Uniform
Maximum time step	DtMax	40 s
Maximum Courant number	CFLMax	0.7
Uniform bottom friction coefficient	UnifFrictCoef	0.025 $s \cdot m^{-1/3}$
Horizontal eddy viscosity (background)	Vicouv	0.1 m^2/s
Horizontal eddy diffusivity (background)	Dicouv	0.1 m^2/s
Smagorinsky constant	Smagorinsky	0.15
Wind drag coefficient type	ICdtvp	4 (Charnock)
Temperature model	Temperature	5 (Complex Ocean Model)
Stanton number (sensible heat transfer)	Stanton	1.3×10^{-3}
Dalton number (latent heat transfer)	Dalton	1.3×10^{-3}
Water clarity depth	Secchidepth	4 m
Turbulence closure model	Turbulencemodel	3 (k–ε model)
Vertical eddy viscosity (background)	Vicoww	5×10^{-5} m^2/s
Vertical eddy diffusivity (background)	Dicoww	5×10^{-6} m^2/s
Equation of state for seawater density	Idensform	2 (UNESCO)

by the Copernicus Marine Environment Monitoring Service (CMEMS).

The tidal model was validated using 2016 observations from 13 tide gauge stations distributed across the Pearl River Estuary, Yangjiang, and the Penghu Islands, demonstrating good agreement with measured tidal levels. In addition, the storm surge model was evaluated using observed surge records from the Chiwan station, confirming its capability to reproduce surge dynamics. The detailed validation results, including time series comparisons, are provided in Supplementary Materials.

2.3. Mangrove drag parameterization

The physical drag effects of mangrove vegetation were incorporated into the model using the Trachytopes extension module embedded within the Delft3D FM system. This module supports the specification of multiple drag classes at sub-grid resolution, enabling a spatially heterogeneous representation of bed roughness. Such functionality is particularly well suited for simulating vegetated coastal ecosystems, such as mangroves (Horstman et al., 2013).

A bed roughness-based approach was adopted to parameterize mangrove-induced drag. Specifically, the drag formulation proposed by Baptist (2005) for submerged vegetation was applied, expressing the total flow resistance as follows:

$$C = \frac{1}{\sqrt{\frac{1}{C_b^2} + \frac{C_D n h_v}{2g}}} + \frac{\sqrt{g}}{\kappa} \ln\left(\frac{h}{h_v}\right) \tag{1}$$

In the above expression, n represents the vegetation density, where m is the number of stems per unit area and D is the mean stem diam. h is the local water depth, h_v is the vegetation height, C_b denotes the bed roughness coefficient, and C_D is the vegetation drag coefficient. When the water depth h approaches the vegetation height h_v, the second term in the equation gradually tends toward zero. In this case, the resistance formula simplifies to the form applicable under emergent or non-submerged vegetation conditions:

$$C = \frac{1}{\sqrt{\frac{1}{C_b^2} + \frac{C_D n h}{2g}}} \tag{2}$$

However, under the bed-based paramization scheme, vegetation significantly increases the equivalent bed roughness, enhancing bed shear stress and sediment transport rates. To account for this additional resistance effect, an extra source term is incorporated into the momentum equation as follows:

$$-\frac{\lambda}{2} u^2 \tag{3}$$

Here, λ characterizes the volumetric drag induced by vegetation. Under non-submerged conditions (i.e., when $h \leq h_v$), the flow resistance and bed roughness can be decoupled and expressed as:

$$C = C_b, \lambda = C_D n \tag{4}$$

In fully submerged conditions (i.e., when $h > h_v$), the bed roughness and vegetation-induced resistance can no longer be easily decoupled. To ensure consistency in the representation of bed shear stress, the following equivalence condition is applied:

$$\frac{u^2}{C^2} = \frac{u_v^2}{C_b^2} \tag{5}$$

In other words, the shear stress computed using the depth-averaged velocity u and the equivalent roughness C should be consistent with that calculated using the within-canopy velocity u_v and the bed roughness C_b. Accordingly, the equivalent roughness coefficient can be expressed as:

$$C = C_b + \frac{\sqrt{g}}{\kappa} \ln\left(\frac{h}{h_v}\right) \sqrt{1 + \frac{C_D n h_v C_b^2}{2g}} \tag{6}$$

The corresponding volumetric drag coefficient is given by:

$$\lambda = C_D n \frac{h_v C_b^2}{h C^2} \tag{7}$$

When $h = h_v$, the above expression simplifies to the standard form presented in Equation (4).

2.4. Experimental scenario design

A series of scenario-based simulations was carried out along the western coastline of Shenzhen. The experiments varied mangrove belt width and drag parameters to evaluate tidal and storm surge responses, with particular focus on Typhoon Mangkhut. Three planting widths, 300 m, 600 m, and 900 m, were selected to reflect common regional restoration practices and to test for potential saturation thresholds in hydrodynamic mitigation. The mangrove drag coefficients used in this study were derived from recent flume experiments conducted by De Dominicis et al. (2023), providing the basis for vegetation parameterization. Detailed parameters for each scenario are listed in Table 2.

As shown in Fig. 2, the intertidal topography was designed from observed tidal variations and regional geomorphology. It was divided into three elevation zones according to tidal inundation patterns: (i) high tidal flats (−0.5 to −1.5 m), which are rarely inundated under normal tides; (ii) mid tidal flats (−1.5 to −2.2 m), which are inundated at high tide and exposed at low tide; (iii) low tidal flats (−2.2 to −3.0 m), which remain submerged for most of the year. Mangrove species were assigned according to ecological traits and local availability in Shenzhen: Bruguiera gymnorhiza and Aegiceras corniculatum in the high- and

Table 2
Mangrove species, belt widths, and associated vegetation parameters used in tidal and Typhoon Mangkhut simulation scenarios.

ID	Location	Width [m]	Mangrove type	h_v [m]	n [1/m]	C_D	C_b [$m^{1/2}/s$]
01	–	–	–	–	–	–	–
02	Intertidal topography	–	–	–	–	–	–
03	Xiwan Mangrove Park	150	Bruguiera gymnorhiza	5	0.30	2	35
		150	Aegiceras corniculatum	4	0.15	2	45
04	Xiwan Mangrove Park	150	Bruguiera gymnorhiza	5	0.30	2	35
		450	Aegiceras corniculatum	4	0.15	2	45
04	Xiwan Mangrove Park	150	Bruguiera gymnorhiza	5	0.30	2	35
		600	Aegiceras corniculatum	4	0.15	2	45
		150	Avicennia marina	6	0.10	2	50
05	Baoan International Airport	150	Bruguiera gymnorhiza	5	0.30	2	35
		150	Aegiceras corniculatum	4	0.15	2	45
06	Baoan International Airport	150	Bruguiera gymnorhiza	5	0.30	2	35
		450	Aegiceras corniculatum	4	0.15	2	45
07	Baoan International Airport	150	Bruguiera gymnorhiza	5	0.30	2	35
		600	Aegiceras corniculatum	4	0.15	2	45
		150	Avicennia marina	6	0.10	2	50

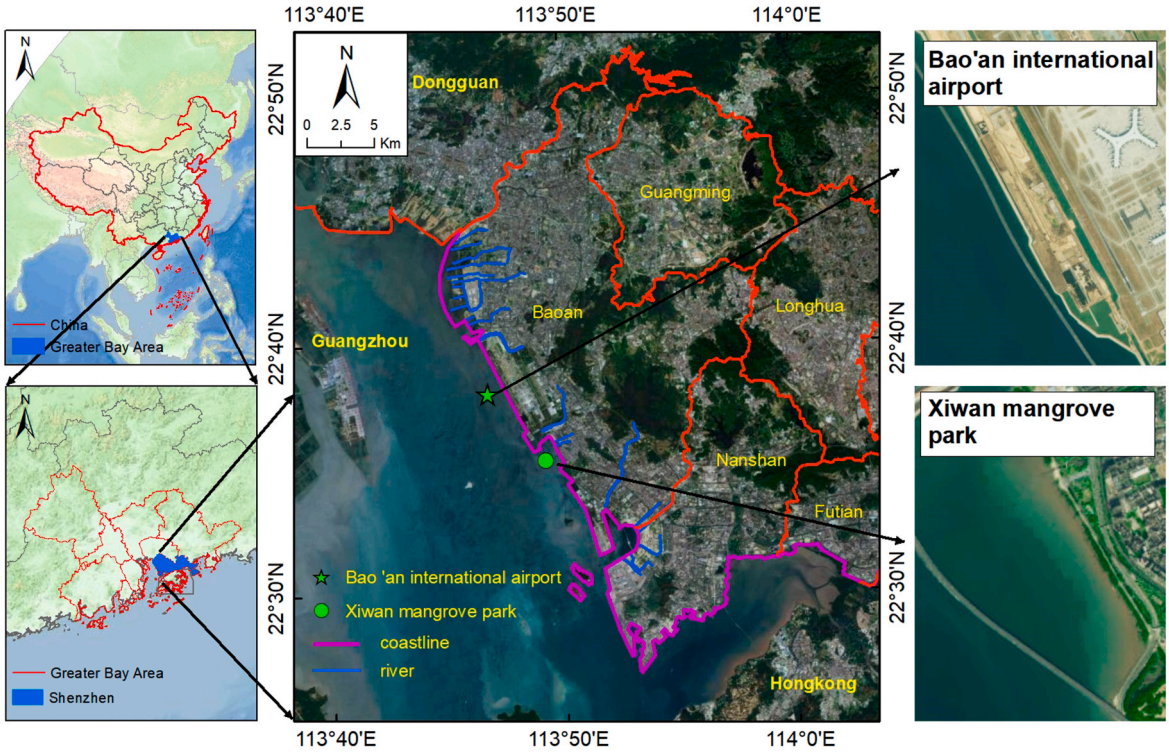

Fig. 1. The study area and the locations of the two representative coastal sites in Shenzhen.

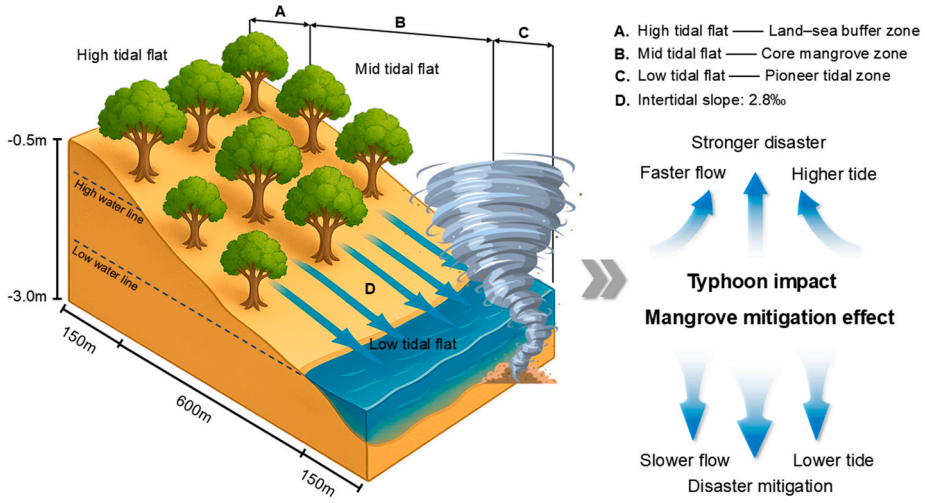

Fig. 2. Schematic diagram of the designed intertidal topography zonation and mangrove belt layout, illustrating their role in mitigating typhoon impacts.

mid-tidal flats, consistent with their typical habitat preferences, and Avicennia marina in the low-tidal flats as a pioneer commonly found at the seaward edge and tolerant of frequent inundation and wave exposure. In the full-coverage scenario, these three zones together yield a total mangrove belt width of 900 m. Elevation decreases from −0.5 m at the landward edge to −3.0 m at the seaward edge; under a linear grade this corresponds to a mean cross-shore slope of approximately 2.8 ‰ (2.5 m over 900 m). The intertidal topography profile is consistent with generalized intertidal morphologies reported in previous studies (Liu et al., 2025).

3. Result

3.1. Hydrodynamic functions of intertidal topography

To evaluate the hydrodynamic role of intertidal topography, comparative simulations were conducted under both tidal and storm surge conditions, with and without the designed intertidal topography. All scenarios excluded mangrove vegetation, enabling a focused assessment of how elevation gradients and bed slope influence coastal flow velocity across the high, mid, and low tidal flats. Fig. 3 illustrates the spatiotemporal variations in average flow velocity across these zones at Xiwan Mangrove Park and the Bao'an Airport coastline under both tidal and Typhoon Mangkhut conditions.

Under tidal forcing, flow velocity exhibited strong spatial variation

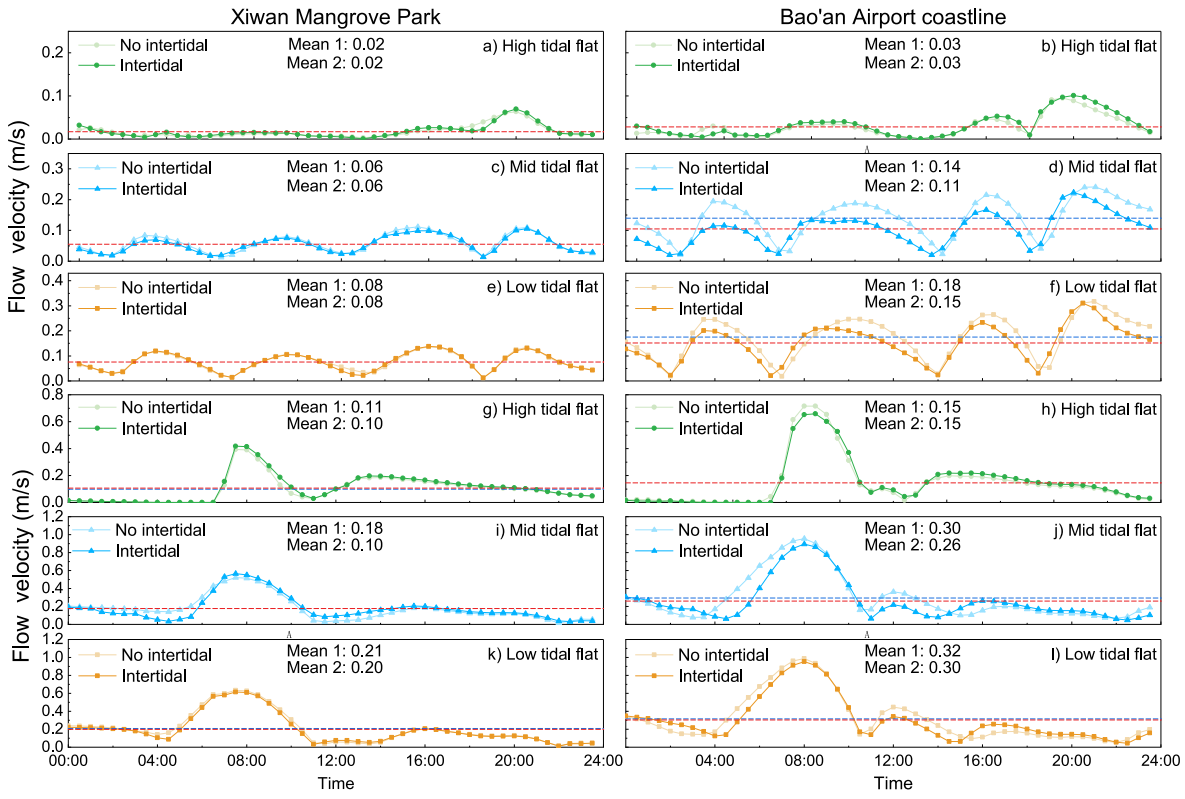

Fig. 3. Time series of depth-averaged flow velocity across the high-, mid-, and low-tidal flats for scenarios with and without intertidal topography, under tidal forcing (a–f) and Typhoon Mangkhut conditions (g–l), all without mangrove vegetation. Xiwan Mangrove Park panels: (a), (c), (e), (g), (i), and (k); Bao'an Airport coastline panels: (b), (d), (f), (h), (j), and (l). Paired curves show the two scenarios; in subplots reporting two mean values, mean-1 and mean-2 correspond to "no intertidal" and "intertidal" scenarios, respectively. The results highlight spatially variable flow reductions attributable to intertidal topography across zones and forcing regimes.

between the two sites. At Xiwan Mangrove Park, introducing the idealized topography led to only minor changes. Average velocities remained around 0.02 m/s, 0.06 m/s, and 0.08 m/s at the high, mid, and low tidal flats, respectively. This limited response reflects the Xiwan Mangrove Park existing natural intertidal topography, which already supports a gradual hydraulic transition. In contrast, the Bao'an Airport coastline demonstrated more substantial reductions due to its originally flat topography, with mid-flat velocity decreasing from 0.14 m/s to 0.11 m/s and low-flat velocity from 0.18 m/s to 0.15 m/s. The high tidal flat showed negligible changes at both sites. This might be because they were not submerged by water under normal tidal conditions.

Under storm-surge conditions associated with Typhoon Mangkhut, the influence of intertidal topography remained evident. At the Bao'an Airport coastline, flow velocity decreased from 0.30 m/s to 0.26 m/s at the mid tidal flat and from 0.32 m/s to 0.30 m/s at the low tidal flat. Xiwan Mangrove Park exhibited a similar trend but with smaller magnitude, consistent with its existing topographic structure. At both locations, the presence of sloped topography delayed flow acceleration and reduced peak velocities, indicating that elevation gradients enhance frictional resistance under extreme forcing.

These results confirm that intertidal topography, particularly in the mid and low tidal flats, can significantly reduce flow velocity. The relative benefits also vary with geomorphic setting. Engineered coastlines such as the Bao'an Airport coastline gain substantial frictional enhancement from added topographic structure, whereas naturally contoured sites such as Xiwan Mangrove Park show only limited improvement because of their inherent buffering capacity.

3.2. *Hydrodynamic functions of mangrove vegetation*

To evaluate the hydrodynamic regulation of mangrove vegetation, simulations were performed under both tidal and storm surge conditions with planting widths of 300 m, 600 m, and 900 m. All scenarios used the same intertidal topography. The objective was to assess changes in flow velocity and water levels across the high, mid, and low tidal flats and to determine whether a threshold exists beyond which additional planting provides diminishing mitigation benefits.

Under tidal conditions, the reduction in flow velocity is influenced by both mangrove planting width and tidal elevation, as shown in Table 3 and Fig. 4.

At Xiwan Mangrove Park, the mid tidal flat exhibited clear reductions with increasing vegetation width. The reduction was 3.48 % at 300 m ($P < 0.001$), 9.51 % at 600 m ($P < 0.001$), and 9.55 % at 900 m ($P < 0.001$), reflecting enhanced attenuation with broader mangrove coverage. The low tidal flat, available only in the 900 m scenario, also showed a 11.30 % reduction. In contrast, the high tidal flat displayed only minor and statistically insignificant changes at all widths ($P > 0.05$), suggesting limited interaction with the flow under regular tidal conditions. At the Bao'an Airport Coastline, reductions were more uniform across tidal zones. The mid tidal flat saw declines of 6.91 %, 7.11 %, and 7.43 % at 300 m, 600 m, and 900 m respectively (all $P < 0.001$). The high tidal flat also exhibited significant reductions across all widths, including 2.15 % at 300 m ($P = 0.036$). The low tidal flat, included only in the 900 m case, showed a reduction of 6.79 % ($P < 0.001$). These spatial patterns are supported by Fig. 4, where flow velocities under mangrove scenarios are consistently lower and more concentrated, particularly in the mid and low tidal zones.

Under storm surge conditions driven by Typhoon Mangkhut, the spatial pattern of flow attenuation shifts significantly, as presented in Table 4 and Fig. 5.

At Xiwan Mangrove Park, the mid tidal flat continued to exhibit increasing reductions with greater planting width. The reductions were 2.39 % at 300 m ($P < 0.001$), 4.39 % at 600 m ($P = 0.0119$), and 4.42 % at 900 m ($P = 0.0054$). The low tidal flat showed a reduction of 2.46 % at

Table 3
Comparison of mean flow velocity reduction under tidal conditions across different mangrove planting widths and tidal zones.

Area	Mangrove planting width (m)	Zone	Current scenario mean (m/s)	Benchmark scenario mean (m/s)	Extent of decline (%)	P-value	Significance
Xiwan Mangrove Park	300	High tidal flat	0.0174	0.0177	1.76	0.0707	ns
		Mid tidal flat	0.0373	0.0387	3.48	<0.001	***
	600	High tidal flat	0.0174	0.0177	1.60	0.0890	ns
		Mid tidal flat	0.0521	0.0576	9.51	<0.001	***
	900	High tidal flat	0.0174	0.0177	1.56	0.0935	ns
		Mid tidal flat	0.0559	0.0618	9.55	<0.001	***
		Low tidal flat	0.0671	0.0757	11.30	<0.001	***
Bao'an Airport Coastline	300	High tidal flat	0.0319	0.0326	2.15	0.0360	*
		Mid tidal flat	0.0845	0.0907	6.91	<0.001	***
	600	High tidal flat	0.0319	0.0326	2.23	0.0311	*
		Mid tidal flat	0.1000	0.1076	7.11	<0.001	***
	900	High tidal flat	0.0318	0.0326	2.26	0.0313	*
		Mid tidal flat	0.1079	0.1165	7.43	<0.001	***
		Low tidal flat	0.1415	0.1518	6.79	<0.001	***

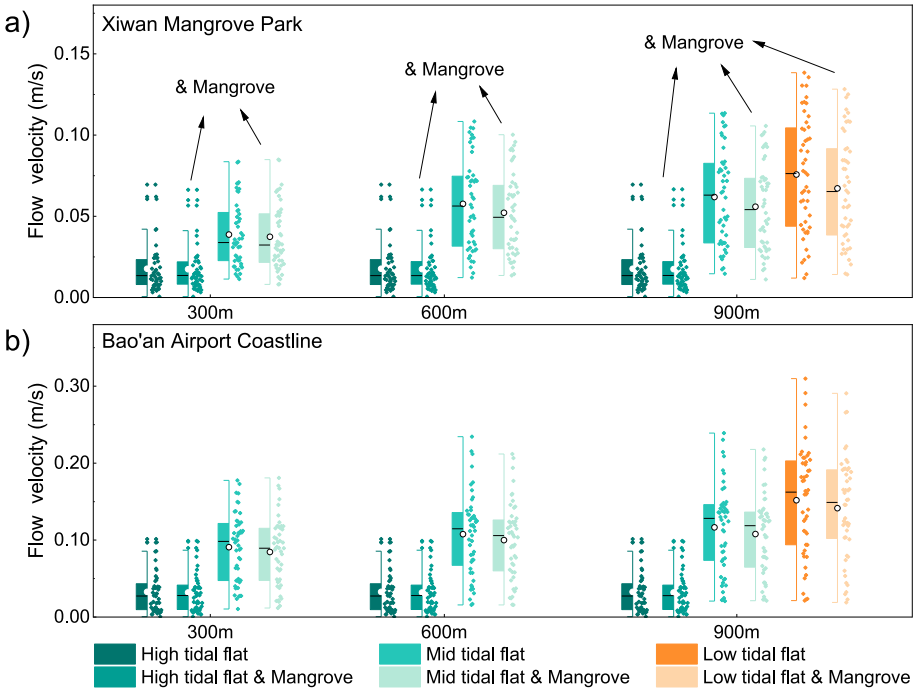

Fig. 4. Influence of Mangrove Belt Width on Flow Velocity Distribution under Tidal Forcing. (a) Xiwan Mangrove Park; (b) Bao'an Airport Coastline. Boxplots illustrate the variation in flow velocity across different tidal zones (high-, mid-, and low-tidal flats) under tidal conditions, corresponding to mangrove belt widths of 300 m, 600 m, and 900 m. White circles represent the mean values, while black horizontal lines denote the medians.

900 m (P = 0.0366). Notably, the high tidal flat experienced consistent and statistically significant reductions across all widths, averaging approximately 9.7–9.8 percent (P < 0.001). At the Bao'an Airport Coastline, attenuation effects were even stronger. The mid tidal flat saw reductions of 2.79 % (P = 0.0450), 3.86 % (P = 0.0040), and 4.11 % (P < 0.001). The high tidal flat showed the most substantial reductions, ranging from 13.08 % to 13.92 % (all P < 0.001). The low tidal flat at 900 m width showed a significant reduction of 4.45 % (P = 0.0021).

Table 4
Comparison of mean flow velocity reduction under typhoon mangkhut storm surge conditions across different mangrove planting widths and tidal zones.

Area	Mangrove planting width (m)	Zone	Current scenario mean (m/s)	Benchmark scenario mean (m/s)	Extent of decline (%)	P-value	Significance
Xiwan Mangrove Park	300	High tidal flat	0.0971	0.1076	9.78	<0.001	***
		Mid tidal flat	0.1389	0.1423	2.39	<0.001	***
	600	High tidal flat	0.0972	0.1076	9.68	<0.001	***
		Mid tidal flat	0.1776	0.1858	4.39	0.0119	*
	900	High tidal flat	0.0970	0.1076	9.84	<0.001	***
		Mid tidal flat	0.1723	0.1803	4.42	0.0054	**
		Low tidal flat	0.1946	0.1995	2.46	0.0366	*
Bao'an Airport Coastline	300	High tidal flat	0.1288	0.1495	13.82	<0.001	***
		Mid tidal flat	0.1826	0.1878	2.79	0.0450	*
	600	High tidal flat	0.1299	0.1495	13.09	<0.001	***
		Mid tidal flat	0.2370	0.2466	3.86	0.0040	**
	900	High tidal flat	0.1287	0.1495	13.92	<0.001	***
		Mid tidal flat	0.2512	0.2620	4.11	<0.001	***
		Low tidal flat	0.2902	0.3037	4.45	0.0021	**

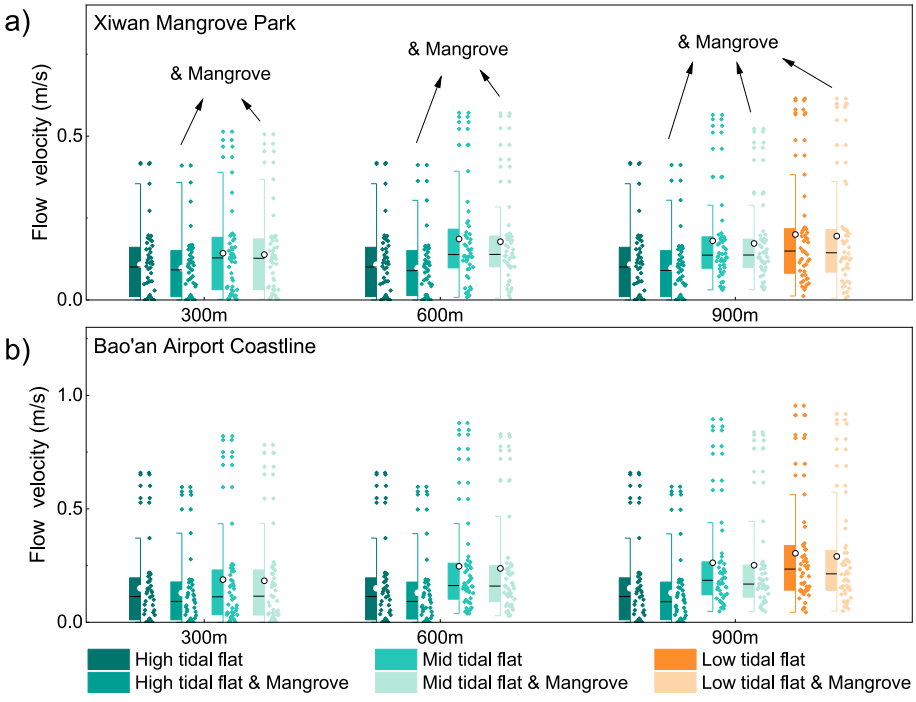

Fig. 5. Influence of Mangrove Belt Width on Flow Velocity Distribution under Typhoon Mangkhut-Induced Storm Surge. (a) Xiwan Mangrove Park; (b) Bao'an Airport Coastal Zone. Boxplots illustrate the variation in flow velocity across different tidal zones (high-, mid-, and low-tidal flats) under storm surge conditions generated by Typhoon Mangkhut, corresponding to mangrove belt widths of 300 m, 600 m, and 900 m. White circles represent the mean values, while black horizontal lines denote the medians.

These effects are evident in Fig. 5, where velocity distributions under vegetated conditions are compressed most in the high tidal zone.

These findings reveal a critical spatial shift in mangrove functioning. Under tidal conditions, flow attenuation is most effective in the mid and low tidal flats. Under storm surge conditions, however, the high tidal flat becomes the primary zone of hydraulic resistance. This shift is likely

associated with elevated water levels during storm surge, which may inundate the high tidal zone and activate the drag effects of mangroves that are otherwise not hydraulically engaged under normal conditions, thereby contributing to greater energy dissipation.

As illustrated in Fig. 6, mangrove planting substantially reduced average maximum water levels under Typhoon Mangkhut conditions at both Xiwan Mangrove Park and the Bao'an Airport coastline. Water level reductions increased progressively with planting widths up to 600 m; however, additional benefits beyond this width were minimal, indicating a saturation threshold in hydrodynamic mitigation effectiveness. Specifically, at Xiwan Mangrove Park, average reductions were 3.85 cm for the 300 m planting scenario, 7.41 cm for 600 m, and only a marginal improvement to 7.43 cm for 900 m. A similar pattern occurred at Bao'an Airport coastline, where average reductions reached 7.32 cm, 15.22 cm, and 15.25 cm for the 300 m, 600 m, and 900 m scenarios, respectively, again highlighting diminishing returns beyond 600 m.

These results suggest that while wider mangrove belts substantially enhance hydrodynamic mitigation up to a certain threshold, further expansion beyond 600 m provides limited additional benefit. This underscores the importance of identifying site-specific saturation points to optimize the cost-effectiveness of large-scale mangrove-based coastal defense strategies.

As shown in Fig. 6b, temporal analysis further revealed contrasting mitigation dynamics between the two sites. Prior to the storm surge peak, the water level reduction curves of Xiwan Mangrove Park showed a declining trend, indicating an early but weakening mitigation effect. In contrast, the curves of the Bao'an Airport coastline rose before the peak, suggesting a delayed but intensifying reduction effect. Notably, the maximum water level reductions did not coincide with the storm surge peak. At Xiwan Mangrove Park, the maximum reduction occurred before the highest surge elevation, whereas at Bao'an Airport coastline it was reached after the surge peak. These contrasting temporal responses primarily reflect differences in the available coastal length for mangrove deployment. The longer shoreline of the Bao'an Airport coastline allows a larger total planting area and consequently stronger mitigation, whereas the shorter shoreline of Xiwan Mangrove Park limits the total vegetated area and its reduction effectiveness.

These findings emphasize that when designing coastal defenses based on mangroves, the spatial scale of planting should be taken into account. Identifying elevation-sensitive thresholds, such as the observed 600 m limit, is essential for optimizing cost-effectiveness and maximizing the hydrodynamic benefits of large-scale nature-based solutions.

3.3. *Site-specific performance: engineered vs. natural coastlines*

Although identical intertidal topography configurations were applied at both study sites, the hydrodynamic outcomes exhibited pronounced spatial heterogeneity due to underlying differences in coastal morphology and shoreline extent. This section compares mitigation performance at two representative locations, Xiwan Mangrove Park with its naturally evolved tidal flat system and the Bao'an Airport coastline with its low-lying engineered shoreline. The analysis focuses on differences in topography responsiveness and mangrove deployment efficacy under Typhoon Mangkhut conditions.

As shown in the first row of Fig. 7, which compares the scenario with designed intertidal topography but without mangrove planting to a baseline without either topographic modification or vegetation, the Bao'an Airport coastline exhibited notably greater reductions in flow velocity. This amplified velocity response can be attributed to the engineered and originally flat shoreline of the Bao'an Airport coastline.

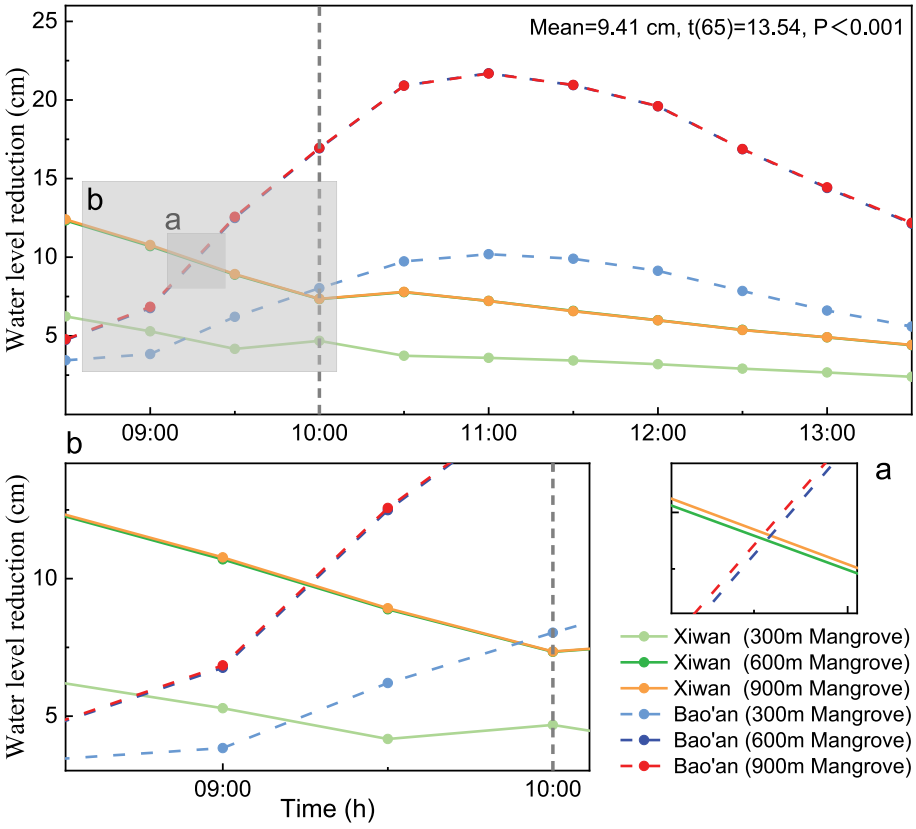

Fig. 6. Temporal evolution of maximum water level reduction under different mangrove planting scenarios at Xiwan Mangrove Park and the Bao'an Airport coastline during Typhoon Mangkhut. Curves show maximum water level reductions relative to the baseline scenario without mangroves for 300 m, 600 m, and 900 m planting widths at Xiwan Mangrove Park and Bao'an Airport coastline. Mean values indicate the average reduction over the simulation period. The gray dashed line indicates the time of peak water level during Typhoon Mangkhut.

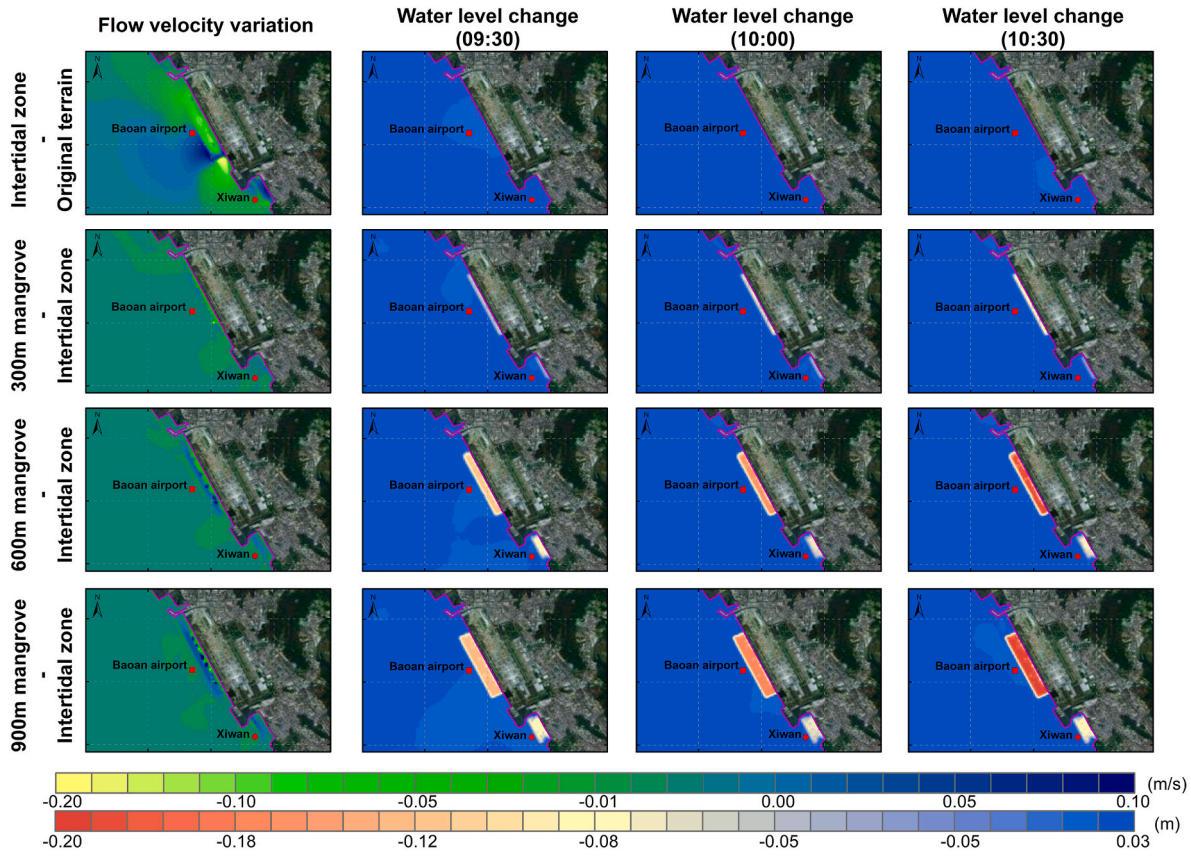

Fig. 7. Relative Contributions of Intertidal Topography and Mangrove Vegetation to Hydrodynamic Mitigation across Six Scenarios. Stacked bars show the percentage contributions of intertidal topography (blue) and mangrove vegetation (green) to reductions in flow velocity and water level. Scenarios (left to right): Xiwan Mangrove Park—tidal flow velocity; Bao'an Airport coastline—tidal flow velocity; Xiwan Mangrove Park—storm-surge flow velocity; Bao'an Airport coastline—storm-surge flow velocity; Xiwan Mangrove Park —storm-surge water level; and Bao'an Airport coastline—storm-surge water level. Symbols indicate average total reduction magnitudes: orange triangles stand for flow velocity reduction and pink squares for water level reduction. (For interpretation of the references to colour in this figure legend, the reader is referred to the Web version of this article.)

Unlike Xiwan Mangrove Park, which already possesses natural elevation gradients and frictional features, the Bao'an Airport coastline lacked inherent resistance. Therefore, the introduction of an idealized intertidal topography increased bed roughness and promoted uniform inundation across tidal zones during storm surges, enabling the artificial topography to effectively dissipate flow energy and enhance hydrodynamic regulation. However, changes in water levels were negligible at both sites, indicating that intertidal topography alone has limited influence on peak water level modulation.

In contrast, the natural topography of Xiwan Mangrove Park already exhibited moderate elevation changes and inherent frictional properties, which provided baseline hydrodynamic resistance. Consequently, the incremental effect of introducing an idealized topography design was comparatively subdued.

The subsequent rows of Fig. 7, which incorporate mangrove planting atop the intertidal topography, further highlight differences in mitigation capacity. The Bao'an Airport coastline, with its longer shoreline and greater available area for mangrove establishment, facilitated broader and more continuous vegetation deployment. This spatial advantage resulted in cohesive and extensive reductions in both flow velocity and water levels under the 600 m and 900 m planting scenarios. Conversely, the relatively shorter coastal stretch of Xiwan Mangrove Park constrained the total vegetated area, leading to more localized attenuation effects despite comparable planting widths.

These results suggest that the effectiveness of nature-based interventions depends not only on the presence of vegetation or topographic modifications but also on the spatial capacity for intervention and the morphological characteristics of the coastal site. Bao'an Airport coastline, while initially more exposed, can achieve substantial hydrodynamic mitigation when supported by purposefully designed topography and adequate vegetation coverage. In contrast, Xiwan Mangrove Park may provide stable baseline resistance but require targeted and spatially efficient strategies to optimize intervention outcomes.

3.4. *Functional contribution quantification*

As shown in Fig. 8, this section quantifies the relative contributions of intertidal topography and mangrove vegetation to hydrodynamic mitigation by calculating their respective impacts on flow velocity and water level reductions under both tidal and Typhoon Mangkhut conditions. The results reveal a clear functional separation. Intertidal topography mainly contributes to flow velocity attenuation, while mangrove vegetation plays the dominant role in regulating water levels.

Across the four scenarios, intertidal topography was the primary contributor to reduction in flow velocity, accounting for 26 %, 69 %, 67 %, and 62 % of the total reduction in the Xiwan Mangrove Park (tidal), Bao'an Airport coastline (tidal), Xiwan Mangrove Park (storm surge), and Bao'an Airport coastline (storm surge) cases, respectively. The comparatively low 26 % contribution at Xiwan under tidal forcing reflects the existing natural intertidal profile, which closely matches the designed topography and therefore provides limited incremental benefit. By contrast, during Typhoon Mangkhut storm surge, the designed intertidal topography accounted for 67 % of the reduction at Xiwan, underscoring its greater influence under stronger hydrodynamic forcing.

The last two scenarios highlight the dominant role of mangrove

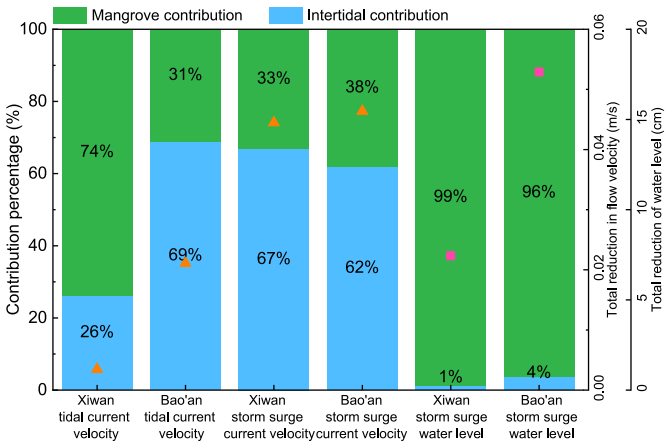

Fig. 8. Relative Contributions of Intertidal Topography and Mangrove Vegetation to Hydrodynamic Mitigation Across Different Scenarios. Stacked bars show the percentage contributions of intertidal topography (blue) and mangrove vegetation (green) to flow velocity and water level reduction under six scenarios, namely Xiwan Mangrove Park tidal flow velocity, Bao'an Airport coastline tidal flow velocity, Xiwan Mangrove Park storm surge flow velocity, Bao'an Airport coastline storm surge flow velocity, Xiwan Mangrove Park storm surge water level, and Bao'an Airport coastline storm surge water level from left to right. The average total reduction magnitudes are indicated by symbols, with orange triangles representing flow velocity reduction and pink squares representing water level reduction. (For interpretation of the references to colour in this figure legend, the reader is referred to the Web version of this article.)

vegetation in reducing water levels under storm surge conditions, contributing 99 % and 96 % of the total effect at Xiwan Mangrove Park and the Bao'an Airport coastline, respectively. These findings indicate that while intertidal topography is critical for attenuating flow velocity, mangrove vegetation becomes the primary factor in reducing peak water levels during extreme events.

It is important to note that these results are based on the 900 m mangrove planting scenario, representing the maximum planting width analyzed. In Fig. 8, average total reduction magnitudes are indicated by symbols—orange triangles for flow-velocity reduction and pink squares for water-level reduction. The results show that reductions are relatively small in the Xiwan Mangrove Park tidal scenario, likely reflecting Xiwan's naturally gentle intertidal slope, which already facilitates gradual flow transitions, together with the lower energy of tidal forcing compared with storm surges. By contrast, a consistent pattern is observed across scenarios: The Bao'an Airport coastline shows greater average reductions than Xiwan Mangrove Park for both flow velocity and water level. This difference is consistent with the Bao'an Airport coastline benefiting more from the intertidal topography design and its longer coastline, which allows a larger total mangrove area and thus stronger overall flow-mitigation effects.

These insights underscore the complementary roles of intertidal topography and mangrove vegetation, highlighting the importance of considering both existing coastal morphology and spatial capacity for planting when designing effective nature-based coastal defenses.

4. Discussion

4.1. Dual mechanisms of nature-based defense

Mangroves, as a widely recognized NbS, play an essential role in enhancing coastal resilience and mitigating hydrodynamic risks (Zhang et al., 2024; Dahdouh-Guebas et al., 2022; Gilani et al., 2021; Herbeck et al., 2020; Wu et al., 2001). In this study, the Delft3D FM system was used to decouple the individual and combined effects of mangrove vegetation and intertidal topography, capturing their influence on both flow velocity and water level under tidal and extreme storm conditions. By stratifying high, mid, and low tidal flats, we identified the distinct functional roles of topography and vegetation and their synergistic interactions.

The results indicate that intertidal topography is the dominant factor in reducing flow velocity under both tidal and storm surge conditions. This effect is particularly evident at the Bao'an Airport coastline, where the addition of intertidal topography significantly enhanced bottom friction and energy dissipation across mid and low tidal flats. At Xiwan Mangrove Park, where natural gradients already exist, the marginal impact of added topography was more subdued. In contrast, mangrove vegetation played a leading role in reducing water levels during Typhoon Mangkhut. Elevated water levels inundated high tidal flats, allowing vegetation-induced drag to become fully engaged. This resulted in a spatial shift in regulatory effectiveness, moving from the mid- and low-tidal flats under normal tidal conditions to the high tidal flats under storm-surge conditions (Zhou et al., 2022b).

4.2. Design thresholds and saturation effects

The quantitative assessment of planting widths at 300 m, 600 m, and 900 m revealed a clear nonlinear response in mitigation performance, indicating a saturation threshold beyond 600 m. At Xiwan Mangrove Park, maximum average water levels dropped by 3.85 cm under the 300 m planting width and further decreased to 7.41 cm at 600 m, while additional planting beyond this width yielded only marginal improvement. A similar trend was observed at the Bao'an Airport coastline, where the 300 m planting scenario resulted in a 7.32 cm reduction in maximum average water level, and the 600 m scenario led to a substantial 15.22 cm decrease, with limited additional gains under the 900 m scenario.

In our Shenzhen case, the marginal benefit of additional planting width declines beyond ~600 m. This diminishing return is plausibly linked to greater submergence of mangrove canopies on the mid- and low-tidal flats under elevated water levels, which weakens effective drag and alters flow resistance dynamics. While the precise threshold will vary with local tidal range, surge levels, platform elevation, vegetation height/density, and bathymetry, the underlying mechanism is general: wider belts do not necessarily yield proportionally larger protective effects. These findings highlight the importance of optimizing (rather than simply maximizing) planting widths in nature-base solutions to balance ecological and protective outcomes with engineering cost-effectiveness. Accordingly, the ~600 m value should be treated as a case-specific reference point, whereas the mechanism offers transferable guidance for identifying site-appropriate critical widths in other coastal settings.

4.3. Consistency with and advancement over previous research

Our findings align with previous studies that highlight the frictional effects of mangrove root structures in shallow zones (high tidal flats) and reduced efficiency in deeper waters (mid and low flats) due to vegetation submergence (van Wesenbeeck et al., 2025). However, many prior works focused exclusively on mangrove belt width or vegetation structure, overlooking the enabling or constraining role of intertidal topography (Xu et al., 2024; Gijón Mancheño et al., 2024; Sandi et al., 2018). Only a few studies have begun to explore this coupled relationship, such as Li et al. (2012), who provided an early numerical assessment of the combined effects of mangroves and tidal flats on storm surge attenuation, showing that tidal flats enhance mangrove-induced flow resistance under typhoon conditions.

However, their approach relied on simplified topography configurations and did not resolve spatial heterogeneity or subdivide the intertidal topography by elevation. In contrast, our study advances this line of research by integrating an idealized but stratified topographic framework with high, mid, and low tidal flats, coupled with vegetation parameterization. This approach allows explicit quantification of the independent and synergistic roles of topography and vegetation under

both tidal and storm surge conditions.

4.4. Toward adaptive and mechanistic NbS modeling

Despite its strengths, this study has several limitations. First, validation under vegetated conditions is constrained by the lack of in situ measurements of flow velocity and vegetation drag during typhoon events. In lieu of direct observations, we adopted a physically based vegetation-drag scheme (Baptist, 2005) with coefficients derived from recent flume experiments (De Dominicis et al., 2023), providing plausible estimates of vegetation-induced resistance. Water-level validation against tide-gauge records shows good agreement, but direct validation of velocity and drag is lacking. Future work should incorporate dedicated field measurements and/or targeted sensitivity analyses to better constrain drag parameters and further improve model realism. Second, mangrove-induced flow reduction can accelerate sediment deposition, triggering elevation feedbacks and promoting long-term expansion (van Bijsterveldt et al., 2023). Thus, vegetation–topography interactions are not static but dynamic over decadal scales.

To advance NbS assessments, future research should: (i) embed morphodynamic feedback modules to capture long-term topographic adjustments (Chen et al., 2025); and (ii) explicitly incorporating climate-change scenarios, including sea-level rise (Dai et al., 2024), changes in storm intensity and frequency, vegetation succession, and compound-flooding interactions, to enhance predictive capability and decision relevance (Hülsen et al., 2024; Chatting et al., 2024; Cai et al., 2022).

It is equally important to account for hurricane-driven mangrove mortality and recovery trajectories (Liang et al., 2025), which influence long-term resilience. Remote sensing and high-resolution monitoring techniques, such as satellite observations and UAV surveys, can provide sustained measurement of vegetation structure and shoreline/elevation changes to support these assessments. Finally, while Typhoon Mangkhut offers a stringent stress test, broader evaluation across multiple storm intensities and tracks is needed to generalize performance and quantify uncertainty (Liu et al., 2013).

5. Conclusion

This study systematically evaluated the synergistic regulation of coastal hydrodynamics by mangrove vegetation and intertidal topography under both tidal and storm surge scenarios. And based on the tidal and storm surge model constructed using the Delft3D FM system we quantified how vegetation-induced drag and topography-induced friction interact across functional tidal zones in two contrasting coastal settings in Shenzhen. These settings include the naturally evolved Xiwan Mangrove Park and the engineered Bao'an Airport coastline.

Our main conclusions are as follows:

1) Dual regulation mechanisms. Intertidal topography plays a dominant role in attenuating flow velocity under both tidal and storm surge conditions, particularly in the mid and low tidal flats. In contrast, mangrove vegetation exerts greater influence on peak water level reduction during extreme events.
2) Functional zone shift under extreme forcing. The zone of maximum mitigation shifts from mid and low flats under tidal conditions to high tidal flats during storm surges, driven by increased inundation depth and canopy engagement.
3) Design threshold for planting width. A mangrove width of 600 m emerges as a critical threshold beyond which additional planting yields diminishing returns. This saturation is attributable to vegetation submergence in deeper zones, which reduces effective drag and informs cost-effective buffer planning.
4) Site-specific performance divergence. Compared with the Xiwan Mangrove Park, the Bao'an Airport coastline, which lack natural frictional features, gain substantial mitigation benefits from added terrain and vegetation.
5) Toward adaptive eco-engineering. To enhance long-term resilience, future work should incorporate sediment–vegetation feedbacks, dynamic topographic evolution, and sea-level rise scenarios. Such integration will support the development of next-generation NbS that are both ecologically grounded and climate-adaptive.

By elucidating the spatial dynamics, performance thresholds, and site-specific interactions governing the synergy between topography and vegetation, this study provides both methodological insights and actionable design principles for advancing nature-based coastal protection in rapidly urbanizing delta regions.

CRediT authorship contribution statement

Rizhong Huang: Writing – review & editing, Writing – original draft, Visualization, Validation, Software, Methodology, Investigation, Formal analysis, Data curation, Conceptualization. **Zhan Tian:** Supervision, Project administration, Funding acquisition, Conceptualization. **Dongli Fan:** Writing – review & editing, Supervision, Conceptualization. **Qinghua Ye:** Methodology. **Qiaodan Liu:** Writing – review & editing. **Ming Kong:** Writing – review & editing. **Yanlong Wang:** Writing – review & editing. **Jiajie Lyu:** Writing – review & editing. **Laixiang Sun:** Writing – review & editing, Conceptualization.

Declaration of competing interest

The authors declare that they have no known competing financial interests or personal relationships that could have appeared to influence the work reported in this paper.

Acknowledgments

This work was supported by the project "Research on the Mechanism of Responses via Multi-scale Interface Processes to Future Extreme Compound Flooding Risks in the Great Bay Area ", funded by the National Natural Science Foundation of China (Grant no. 42430407).

Appendix A. Supplementary data

Supplementary data to this article can be found online at https://doi.org/10.1016/j.ocecoaman.2025.108004.

Data availability

Data will be made available on request.

References

Ai, B., Ma, C., Zhao, J., Zhang, R., 2020. The impact of rapid urban expansion on coastal mangroves: a case study in Guangdong Province, China. Front. Earth Sci. 14 (1), 37–49. https://doi.org/10.1007/s11707-019-0768-6.

Alongi, D.M., 2008. Mangrove forests: resilience, protection from tsunamis, and responses to global climate change. Estuar. Coast Shelf Sci. 76 (1), 1–13. https://doi.org/10.1016/j.ecss.2007.08.024.

Baptist, M., 2005. Modelling Floodplain Beiogemomorphology. Delft University Press.

Bouillon, S., Borges, A.V., Castañeda-Moya, E., Diele, K., Dittmar, T., Duke, N.C., Kristensen, E., Lee, S.Y., Marchand, C., Middelburg, J.J., Rivera-Monroy, V.H., Smith, T.J., Twilley, R.R., 2008. Mangrove production and carbon sinks: a revision of global budget estimates. Glob. Biogeochem. Cycles 22 (2), 2007GB003052. https://doi.org/10.1029/2007GB003052.

Cai, R., Ding, R., Yan, X., Li, C., Sun, J., Tan, H., Men, W., Guo, H., Wang, C., 2022. Adaptive response of Dongzhaigang mangrove in China to future sea level rise. Sci. Rep. 12 (1), 11495. https://doi.org/10.1038/s41598-022-15774-7.

Chan, F.K.S., Yang, L.E., Scheffran, J., Mitchell, G., Adekola, O., Griffiths, J., Chen, Y., Li, G., Lu, X., Qi, Y., Li, L., Zheng, H., McDonald, A., 2021. Urban flood risks and emerging challenges in a Chinese delta: the case of the Pearl River Delta. Environ. Sci. Pol. 122, 101–115. https://doi.org/10.1016/j.envsci.2021.04.009.

Chang, C., Mori, N., Tsuruta, N., Suzuki, K., Yanagisawa, H., 2022. An experimental study of mangrove-induced resistance on water waves considering the impacts of

typical *Rhizophora* roots. J. Geophys. Res.: Oceans 127 (6), e2022JC018653. https://doi.org/10.1029/2022JC018653.
Chatting, M., Al-Maslamani, I., Walton, M., Skov, M.W., Kennedy, H., Husrevoglu, S., Le Vay, L., 2024. Past, present and future global mangrove primary productivity. Sci. Total Environ. 957, 177446. https://doi.org/10.1016/j.scitotenv.2024.177446.
Chen, Q., Li, Y., Kelly, D.M., Zhang, K., Zachry, B., Rhome, J., 2021. Improved modeling of the role of mangroves in storm surge attenuation. Estuar. Coast Shelf Sci. 260, 107515. https://doi.org/10.1016/j.ecss.2021.107515.
Chen, X., Zhang, F., Lao, Y., Wang, X., Du, J., Santos, I.R., 2018. Submarine groundwater discharge-derived carbon fluxes in mangroves: an important component of blue carbon budgets? J. Geophys. Res.: Oceans 123 (9), 6962–6979. https://doi.org/10.1029/2018JC014448.
Chen, R., Long, C., Dai, Z., Mei, X., Cheng, J., 2025. Spatiotemporal dynamics of mangrove ecosystems in the Mai Po Nature Reserve Ramsar site: drivers, challenges, and implications. Ocean Coast Manag. 270, 107904. https://doi.org/10.1016/j.ocecoaman.2025.107904.
Dai, Z., Long, C., Mei, X., Fagherazzi, S., Xiong, Y., 2024. Overestimation of mangroves deterioration from sea level rise in tropical deltas. Geophys. Res. Lett. 51 (19), e2024GL109675. https://doi.org/10.1029/2024GL109675.
Dahdouh-Guebas, F., Friess, D.A., Lovelock, C.E., Connolly, R.M., Feller, I.C., Rogers, K., Cannicci, S., 2022. Cross-cutting research themes for future mangrove forest research. Nat. Plants 8 (10), 1131–1135. https://doi.org/10.1038/s41477-022-01245-4.
Das, S., Vincent, J.R., 2009. Mangroves protected villages and reduced death toll during Indian super cyclone. Proc. Natl. Acad. Sci. 106 (18), 7357–7360. https://doi.org/10.1073/pnas.0810440106.
De Dominicis, M., Wolf, J., Jevrejeva, S., Zheng, P., Hu, Z., 2020. Future interactions between sea level rise, tides, and storm surges in the world's largest urban area. Geophys. Res. Lett. 47 (4), e2020GL087002. https://doi.org/10.1029/2020GL087002.
De Dominicis, M., Wolf, J., Van Hespen, R., Zheng, P., Hu, Z., 2023. Mangrove forests can be an effective coastal defence in the Pearl River Delta, China. Commun. Earth Environ. 4 (1), 13. https://doi.org/10.1038/s43247-022-00672-7.
Emanuel, K., 2005. Increasing destructiveness of tropical cyclones over the past 30 years. Nature 436 (7051), 686–688. https://doi.org/10.1038/nature03906.
Gijón Mancheño, A., Vuik, V., Van Wesenbeeck, B.K., Jonkman, S.N., Van Hespen, R., Moll, J.R., Kazi, S., Urrutia, I., Van Ledden, M., 2024. Integrating mangrove growth and failure in coastal flood protection designs. Sci. Rep. 14 (1), 7951. https://doi.org/10.1038/s41598-024-58705-4.
Gilani, H., Naz, H.I., Arshad, M., Nazim, K., Akram, U., Abrar, A., Asif, M., 2021. Evaluating mangrove conservation and sustainability through spatiotemporal (1990–2020) mangrove cover change analysis in Pakistan. Estuar. Coast Shelf Sci. 249, 107128. https://doi.org/10.1016/j.ecss.2020.107128.
Gilman, E.L., Ellison, J., Duke, N.C., Field, C., 2008. Threats to mangroves from climate change and adaptation options: a review. Aquat. Bot. 89 (2), 237–250. https://doi.org/10.1016/j.aquabot.2007.12.009.
Hagger, V., Worthington, T.A., Lovelock, C.E., Adame, M.F., Amano, T., Brown, B.M., Friess, D.A., Landis, E., Mumby, P.J., Morrison, T.H., O'Brien, K.R., Wilson, K.A., Zganjar, C., Saunders, M.I., 2022. Drivers of global mangrove loss and gain in social-ecological systems. Nat. Commun. 13 (1), 6373. https://doi.org/10.1038/s41467-022-33962-x.
Hallegatte, S., Green, C., Nicholls, R.J., Corfee-Morlot, J., 2013. Future flood losses in major coastal cities. Nat. Clim. Change 3 (9), 802–806. https://doi.org/10.1038/nclimate1979.
Herbeck, L.S., Krumme, U., Andersen, T.J., Jennerjahn, T.C., 2020. Decadal trends in mangrove and pond aquaculture cover on Hainan (China) since 1966: mangrove loss, fragmentation and associated biogeochemical changes. Estuar. Coast Shelf Sci. 233, 106531. https://doi.org/10.1016/j.ecss.2019.106531.
Hochard, J.P., Hamilton, S., Barbier, E.B., 2019. Mangroves shelter coastal economic activity from cyclones. Proc. Natl. Acad. Sci. 116 (25), 12232–12237. https://doi.org/10.1073/pnas.1820067116.
Horstman, E., Dohmen-Janssen, M., Hulscher, S., 2013. Modeling tidal dynamics in a mangrove creek catchment in Delft3D. Coastal Dynamics.
Horstman, E.M., Dohmen-Janssen, C.M., Narra, P.M.F., Van Den Berg, N.J.F., Siemerink, M., Hulscher, S.J.M.H., 2014. Wave attenuation in mangroves: a quantitative approach to field observations. Coast. Eng. 94, 47–62. https://doi.org/10.1016/j.coastaleng.2014.08.005.
Hu, W., Wang, Y., Zhang, D., Yu, W., Chen, G., Xie, T., Liu, Z., Ma, Z., Du, J., Chao, B., Lei, G., Chen, B., 2020. Mapping the potential of mangrove forest restoration based on species distribution models: a case study in China. Sci. Total Environ. 748, 142321. https://doi.org/10.1016/j.scitotenv.2020.142321.
Hülsen, S., Dee, L., Kropf, C., Meiler, S., Bresch, D., 2024. Mangroves and their services are at risk from tropical cyclones and sea level rise under climate change. https://doi.org/10.21203/rs.3.rs-5346064/v1.
Kiesel, J., MacPherson, L.R., Schuerch, M., Vafeidis, A.T., 2022. Can managed realignment buffer extreme surges? The relationship between Marsh Width, vegetation cover and surge attenuation. Estuaries Coasts 45 (2), 345–362. https://doi.org/10.1007/s12237-021-00984-5.
Krauss, K.W., McKee, K.L., Lovelock, C.E., Cahoon, D.R., Saintilan, N., Reef, R., Chen, L., 2014. How mangrove forests adjust to rising sea level. New Phytol. 202 (1), 19–34. https://doi.org/10.1111/nph.12605.
Liang, X., Dai, Z., Mei, X., Wang, R., Zeng, W., Fagherazzi, S., 2025. Hurricanes induced irreversible large-scale loss of mangrove forests. Geophys. Res. Lett. 52 (9), e2025GL115692. https://doi.org/10.1029/2025GL115692.
Liu, S., Hu, Z., Grandjean, T.J., Wang, Z.B., Van Zelst, V.T.M., Qi, L., Xu, T., Seo, J.Y., Bouma, T.J., 2025. Dynamics and drivers of tidal flat morphology in China. Nat. Commun. 16 (1), 2153. https://doi.org/10.1038/s41467-025-57525-y.
Lagomasino, D., Fatoyinbo, T., Castañeda-Moya, E., Cook, B.D., Montesano, P.M., Neigh, C.S.R., Corp, L.A., Ott, L.E., Chavez, S., Morton, D.C., 2021. Storm surge and ponding explain mangrove dieback in southwest Florida following Hurricane Irma. Nat. Commun. 12 (1), 4003. https://doi.org/10.1038/s41467-021-24253-y.
Li, L., Wang, X.H., Williams, D., Sidhu, H., Song, D., 2012. Numerical study of the effects of mangrove areas and tidal flats on tides: a case study of Darwin Harbour, Australia. J. Geophys. Res.: Oceans 117 (C6), 2011JC007494. https://doi.org/10.1029/2011JC007494.
Liu, H., Zhang, K., Li, Y., Xie, L., 2013. Numerical study of the sensitivity of mangroves in reducing storm surge and flooding to hurricane characteristics in southern Florida. Cont. Shelf Res. 64, 51–65. https://doi.org/10.1016/j.csr.2013.05.015.
Maza, M., Adler, K., Ramos, D., Garcia, A.M., Nepf, H., 2017. Velocity and drag evolution from the leading edge of a model mangrove forest. J. Geophys. Res.: Oceans 122 (11), 9144–9159. https://doi.org/10.1002/2017JC012945.
Maza, M., Lara, J.L., Losada, I.J., 2019. Experimental analysis of wave attenuation and drag forces in a realistic fringe Rhizophora mangrove forest. Adv. Water Resour. 131, 103376. https://doi.org/10.1016/j.advwatres.2019.07.006.
Mazda, Y., Magi, M., Ikeda, Y., Kurokawa, T., Asano, T., 2006. Wave reduction in a mangrove forest dominated by Sonneratia sp. Wetl. Ecol. Manag. 14 (4), 365–378. https://doi.org/10.1007/s11273-005-5388-0.
Mazda, Y., Magi, M., Kogo, M., Hong, O.P., 1997. Mangroves as coastal protection from waves in the Tong King delta, Vietnam. Mangroves Salt Marshes 1, 127–135. https://doi.org/10.1023/A:1009928003700.
Menéndez, P., Losada, I.J., Torres-Ortega, S., Narayan, S., Beck, M.W., 2020. The global flood protection benefits of mangroves. Sci. Rep. 10 (1), 4404. https://doi.org/10.1038/s41598-020-61136-6.
Menéndez, P., Losada, I.J., Torres-Ortega, S., Toimil, A., Beck, M.W., 2019. Assessing the effects of using high-quality data and high-resolution models in valuing flood protection services of mangroves. PLoS One 14 (8), e0220941. https://doi.org/10.1371/journal.pone.0220941.
Peng, Y., Zheng, M., Zheng, Z., Wu, G., Chen, Y., Xu, H., Tian, G., Peng, S., Chen, G., Lee, S.Y., 2016. Virtual increase or latent loss? A reassessment of mangrove populations and their conservation in Guangdong, southern China. Mar. Pollut. Bull. 109 (2), 691–699. https://doi.org/10.1016/j.marpolbul.2016.06.083.
Reguero, B.G., Beck, M.W., Bresch, D.N., Calil, J., Meliane, I., 2018. Comparing the cost effectiveness of nature-based and coastal adaptation: a case study from the Gulf Coast of the United States. PLoS One 13 (4), e0192132. https://doi.org/10.1371/journal.pone.0192132.
Sandi, S.G., Rodríguez, J.F., Saintilan, N., Riccardi, G., Saco, P.M., 2018. Rising tides, rising gates: the complex ecogeomorphic response of coastal wetlands to sea-level rise and human interventions. Adv. Water Resour. 114, 135–148. https://doi.org/10.1016/j.advwatres.2018.02.006.
Sasmito, S.D., Taillardat, P., Adinugroho, W.C., Krisnawati, H., Novita, N., Fatoyinbo, L., Friess, D.A., Page, S.E., Lovelock, C.E., Murdiyarso, D., Taylor, D., Lupascu, M., 2025. Half of land use carbon emissions in Southeast Asia can be mitigated through peat swamp forest and mangrove conservation and restoration. Nat. Commun. 16 (1), 740. https://doi.org/10.1038/s41467-025-55892-0.
Smolders, S., Plancke, Y., Ides, S., Meire, P., Temmerman, S., 2015. Role of intertidal wetlands for tidal and storm tide attenuation along a confined estuary: a model study. Nat. Hazards Earth Syst. Sci. 15 (7), 1659–1675. https://doi.org/10.5194/nhess-15-1659-2015.
Stark, J., Plancke, Y., Ides, S., Meire, P., Temmerman, S., 2016. Coastal flood protection by a combined nature-based and engineering approach: modeling the effects of marsh geometry and surrounding dikes. Estuar. Coast Shelf Sci. 175, 34–45. https://doi.org/10.1016/j.ecss.2016.03.027.
Su, J., Friess, D.A., Gasparatos, A., 2021. A meta-analysis of the ecological and economic outcomes of mangrove restoration. Nat. Commun. 12 (1), 5050. https://doi.org/10.1038/s41467-021-25349-1.
Temmerman, S., Meire, P., Bouma, T.J., Herman, P.M.J., Ysebaert, T., De Vriend, H.J., 2013. Ecosystem-based coastal defence in the face of global change. Nature 504 (7478), 79–83. https://doi.org/10.1038/nature12859.
Van Bijsterveldt, C.E.J., Herman, P.M.J., Van Wesenbeeck, B.K., Ramadhani, S., Heuts, T. S., Van Starrenburg, C., Tas, S.A.J., Triyanti, A., Helmi, M., Tonneijck, F.H., Bouma, T.J., 2023. Subsidence reveals potential impacts of future sea level rise on inhabited mangrove coasts. Nat. Sustain. 6 (12), 1565–1577. https://doi.org/10.1038/s41893-023-01226-1.
Van Wesenbeeck, B.K., Van Zelst, V.T.M., Antolinez, J.A.A., De Boer, W.P., 2025. Quantifying uncertainty in wave attenuation by mangroves to inform coastal green belt policies. Commun. Earth Environ. 6 (1), 258. https://doi.org/10.1038/s43247-025-02178-4.
Wang, H., Peng, Y., Wang, C., Wen, Q., Xu, J., Hu, Z., Jia, X., Zhao, X., Lian, W., Temmerman, S., Wolf, J., Bouma, T., 2021. Mangrove loss and gain in a densely populated urban Estuary: lessons from the Guangdong-Hong Kong-Macao Greater Bay Area. Front. Mar. Sci. 8, 693450. https://doi.org/10.3389/fmars.2021.693450.
Ward, P.J., Couasnon, A., Eilander, D., Haigh, I.D., Hendry, A., Muis, S., Veldkamp, T.I. E., Winsemius, H.C., Wahl, T., 2018. Dependence between high sea-level and high river discharge increases flood hazard in global deltas and estuaries. Environ. Res. Lett. 13 (8), 084012. https://doi.org/10.1088/1748-9326/aad400.
Wei, L., Lin, F., Gao, J., Rugema, J., Akram, W., Wang, Y., 2025. Complexity of leaf trait covariation for mangrove species. Npj Biodiversity 4 (1), 6. https://doi.org/10.1038/s44185-025-00077-7.
Wei, S., Zhang, H., Xu, Z., Lin, G., Lin, Y., Liang, X., Ling, J., Wee, A.K.S., Lin, H., Zhou, Y., Gong, P., 2024. Coastal urbanization may indirectly positively impact

growth of mangrove forests. Commun. Earth Environ. 5 (1), 608. https://doi.org/10.1038/s43247-024-01776-y.

Wu, Y., Falconer, R.A., Struve, J., 2001. Mathematical modelling of tidal currents in mangrove forests. Environ. Model. Software 16 (1), 19–29. https://doi.org/10.1016/S1364-8152(00)00059-1.

Xu, X., Fu, D., Su, F., Lyne, V., Yu, H., Tang, J., Hong, X., Wang, J., 2024. Global distribution and decline of mangrove coastal protection extends far beyond area loss. Nat. Commun. 15 (1), 10267. https://doi.org/10.1038/s41467-024-54349-0.

Zhou, X., Dai, Z., Carniello, L., Long, C., Wang, R., Luo, J., Huang, Z., 2022a. Linkage between mangrove wetland dynamics and wave attenuation during a storm–a case study of the Nanliu Delta, China. Mar. Geol. 454, 106946. https://doi.org/10.1016/j.margeo.2022.106946.

Zhou, X., Dai, Z., Pang, W., Wang, J., Long, C., 2022b. Wave attenuation over mangroves in the nanliu Delta, China. Front. Mar. Sci. 9, 874818. https://doi.org/10.3389/fmars.2022.874818.

Zhang, J., Gan, S., Yang, P., Zhou, J., Huang, X., Chen, H., He, H., Saintilan, N., Sanders, C.J., Wang, F., 2024. A global assessment of mangrove soil organic carbon sources and implications for blue carbon credit. Nat. Commun. 15 (1), 8994. https://doi.org/10.1038/s41467-024-53413-z.

Zhang, J., Lu, Z., Zhou, J., Qin, G., Bai, Y., Sanders, C.J., Macreadie, P.I., Yuan, J., Huang, X., Wang, F., 2025. Getting the best of carbon bang for mangrove restoration buck. Nat. Commun. 16 (1), 1297. https://doi.org/10.1038/s41467-025-56587-2.

Zhang, K., Liu, H., Li, Y., Xu, H., Shen, J., Rhome, J., Smith, T.J., 2012. The role of mangroves in attenuating storm surges. Estuar. Coast Shelf Sci. 102–103, 11–23. https://doi.org/10.1016/j.ecss.2012.02.021.